REVIEWS OF TOPICAL PROBLEMS

Resonance effects in photonic crystals and metamaterials

(100th anniversary of the Ioffe Institute)

M V Rybin, M F Limonov

Contents

Abstract. We review experimental and theoretical studies of resonance effects in electromagnetic spectra of various photonic structures. We briefly present the history of research areas related to photonic crystals and metamaterials. Considered initially as two different classes of human-made objects, they are now more and more frequently analyzed from a common perspective. We focus on the phase transition between the photonic crystal and metamaterial, which is accompanied by the emergence of negative permeability in a purely dielectric 2D structure. The main mechanisms that drive the resonant processes related to extended (i.e., nonlocal) Bragg resonances in photonic crystals and local resonances on individual structural elements of metamaterials are considered. We discuss in detail the electromagnetic properties of weakly absorbing dielectric particles with a high refractive index that exhibit, in addition to electrical resonances, intensive magnetic Mie resonances. The importance of this area is determined by the vast amount of research that aims to create the elemental base of photonics.

M V Rybin[(*)], **M F Limonov**
Ioffe Institute,
ul. Politekhnicheskaya 26, 194021 St. Petersburg, Russian Federation
E-mail: [(*)] m.rybin@mail.ioffe.ru

1. Introduction

The 20th century, which can be considered the electronic century, has clearly demonstrated that extremal physical properties in both living nature and human-made devices are especially distinctly manifested under resonance conditions. Communications, TV, lasers, computers, the Internet — all this operates thanks to various resonance elements. However, by the end of the 20th century, most of the standard materials had been investigated in detail and devices and mechanisms based on them reached their limiting, theoretically possible, parameters. Such materials could no longer meet the challenges of the new 21st century and could not support the constantly increasing requirements of the photonics, electronics, medicine, sensorics, and high-tech innovative industries and innovation industrial sectors. It was expected that further progress would be related to the creation of fundamentally new technologies and materials which would have unique resonance (electromagnetic, acoustic, mechanical, etc.) properties due to their nontrivial structure and composition, the specific features of their photonic and electronic band structure, the spatial dispersion of physical properties, and miniaturization and size effects.

Thus, it is not surprising that at the turn of the 20th and 21st centuries two new classes of human-made materials with distinct resonance properties were created: photonic crystals (PCs) and metamaterials (MMs). The significant difference between these classes of materials is that the functional properties of PCs are based on extended (i.e., nonlocal) Bragg resonances of the structure as a whole, whereas MM properties are determined by local resonances on individual structural elements.

It is customary to date the beginning of photonic crystal studies dates to 1987, when Yablonovitch and John published papers [1, 2] devoted to the investigation of artificial structures in which the modulation period of the permittivity is comparable to the period of a probe electromagnetic wave. Such structures were later also called 'semiconductors for light', because theoretical and experimental approaches developed for studying electrons in semiconductors were successfully applied for describing electromagnetic waves propagating in PCs. The concepts of the band structure, localization, superlattice, and impurity states became the fundamental base for developing the theory of interaction of light with PCs. The PC topic is considered in Section 2.

Note that the history of PC studies actually originated back in the 19th century, when Rayleigh published the fundamentals of the theory of electromagnetic wave propagation in one-dimensional periodic structures, i.e., in fact, in one-dimensional PCs [3]. In 1972, Bykov considered the problem of spontaneous radiation in periodic media with forbidden bands [4]. However, these studies were ahead of their time and did not receive the appropriate scientific resonance.

The development and study of MMs is related to the name Pendry, who published papers [5, 6] devoted to investigations of artificial composite structures consisting of elements with dimensions considerably smaller than the operating wavelength and having resonance properties at this wavelength [7–10]. The propagation of light in MMs, unlike its propagation in PCs, can be described in a conventional way using material parameters such as the permittivity ε and permeability μ, which are related to the electric and magnetic responses of individual structural elements.

Correctly selected and spatially ordered structural elements make it possible to create MMs with the desired values of ε and μ, including negative values, thereby constructing left-handed media which were described by Veselago on the pages of *Sov. Phys. Usp.* [11] back in the middle of the 20th century. By selecting parameters ε and μ properly, we can create MMs having a number of unique properties, which until recently belonged to the field of science fiction and are now realized or nearly realized in practice. They are optical magnetism [12], a plane superlens overcoming the diffraction limit [13], and a hyperlens magnifying an image with details also overcoming the diffraction limit of resolution of standard lenses [14]. One of the most discussed application fields of MMs is the invisibility and masking of objects — the possibility of making objects invisible in certain spectral ranges [15–17]. Metamaterials are already used in antennas, sensors, and absorbers [18–21].

Metamaterials were initially created based on metal subwavelength periodic structures [5, 22–26]. In particular, the first MMs were prepared for the microwave range, and their resonance elements were split-ring resonators made of metal wires. Unfortunately, in the visible range, such structures lose their functional properties because of plasmon resonance and large ohmic losses. In 2002, O'Brien and Pendry [27] theoretically demonstrated the MM properties (the negative magnetic susceptibility) of purely dielectric compounds with a high permittivity. They considered a square two-dimensional lattice formed by homogeneous dielectric cylinders and showed that the MM properties in this structure appear due to Mie resonances with a pronounced magnetic response. The development and study of all-dielectric MMs in recent time is attracting great interest [28–32]. The use of dielectric MMs (in particular, silicon [33] in the optical frequency range) instead of classic plasmon structures reduces ohmic losses and allows one to control not only the electric but also the magnetic component of a light wave, thereby increasing the total light control efficiency in nanoscaled structures.

Although the number of publications on PCs and MMs is continually increasing, these two classes of photonic structures are considered in most original papers, reviews, and monographs [8–10, 37, 38] independently of each other. The aim of our review is to fill this significant gap and to describe in one publication the fundamental resonance properties of both PCs and MMs important for applications. In Section 5, we directly bridge these two classes of human-made structures by discussing the PC–MM phase transition. The idea of such a transition is based on the dualism of dielectric periodic lattices which, depending on the crystal parameters (symmetry, lattice constant–probe wavelength ratio, permittivity) can belong to either the PC or the MM class [39]. The study of physical processes governing this photonic phase transition should not only expand fundamental knowledge but also play an important role in the development of artificial materials with new functional properties which can replace semiconductor devices in all-optical communications and data processing systems.

2. Photonic crystals

Photonic crystals are weakly absorbing structures with the permittivity periodically modulated with a period comparable to an electromagnetic wavelength in the spectral range under study. The periodic modulation of the permittivity produces alternating bands of allowed states (eigenstates) and forbidden ones. Depending on the crystal structure symmetry and the permittivity modulation depth, either stop-bands (gaps in the eigenstate spectrum for light propagating in a certain direction in the PC lattice) or a complete photonic band gap formed by overlapped stop-bands over all propagation directions of light, irrespective of its polarization can be formed.

The formation of band gaps is related to extended (i.e., nonlocal) Bragg resonances of the crystal lattice. Bragg scattering [40] providing the basis for the formation of band gaps in the spectra of wave states of different types (electron, phonon, photonic, magnon) was discovered in X-ray scattering experiments with natural (atomic) crystals. From the discovery of X-ray Bragg scattering in 1912 to the advent of PCs, i.e., structures with functional properties based on Bragg scattering in the optical range, eight decades elapsed. Such a large time period is probably explained by the fact that the band gap is related to the dielectric contrast $\eta = \max \varepsilon(\mathbf{r})/\min \varepsilon(\mathbf{r})$, which in the X-ray region for natural crystals is only $\eta \approx 1 \times 10^{-5}$, whereas a complete photonic band gap can exist only if $\eta > 4$ [38]. Artificial structures with such a high dielectric contrast were created only recently.

2.1 Bragg resonances
in three-dimensional ordered photonic crystals
The characteristic lattice period a in PCs is comparable to the probe wavelength λ. In the case of low-contrast crystals, the intrinsic (local) resonances of individual structural elements (for example, the Mie resonances of spherical particles) lie considerably higher than the spectral region studied in PCs,
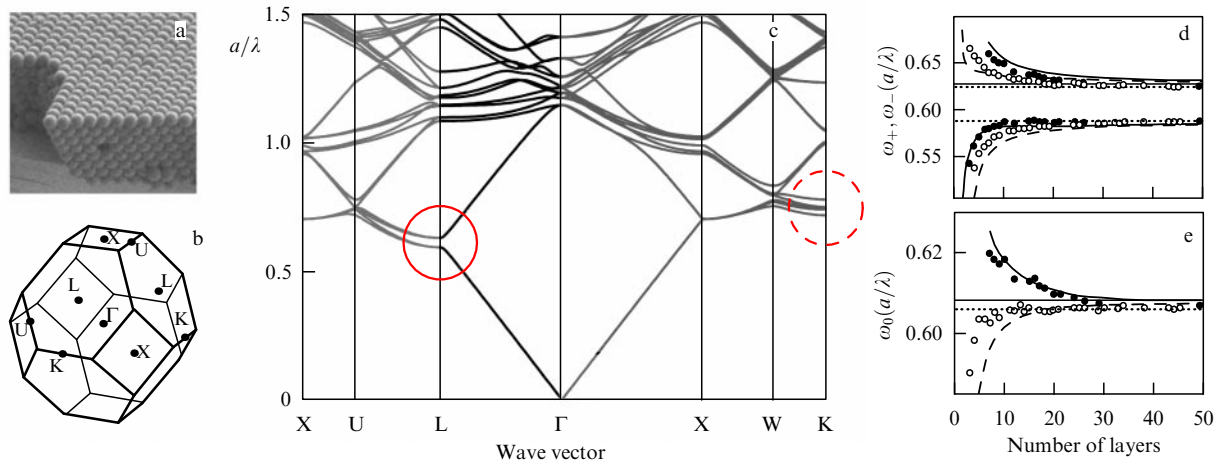
Figure 1. (a) Scanning electron microscopy (SEM) image of a synthetic opal sample (adapted from [34]). (b) Brillouin zone of an fcc structure [35]. (c) Photonic band diagram of the fcc structure of polystyrene opal. The $\Gamma-L$ direction (corresponding to the [111] growth direction) is shown by thick lines [35]. (d) Dots are experimentally determined edges ω_+ and ω_- of the (111) reflection peak at its FWHM as functions of the number of monolayers. Curves are calculated by the method of plane waves in the scalar approximation [36]. (e) Experimental (dots) and calculated (curves) positions of the center ω_0 of the (111) reflection line as functions of the number of monolayers. Results are obtained for the opal structure consisting of polystyrene spheres [36].
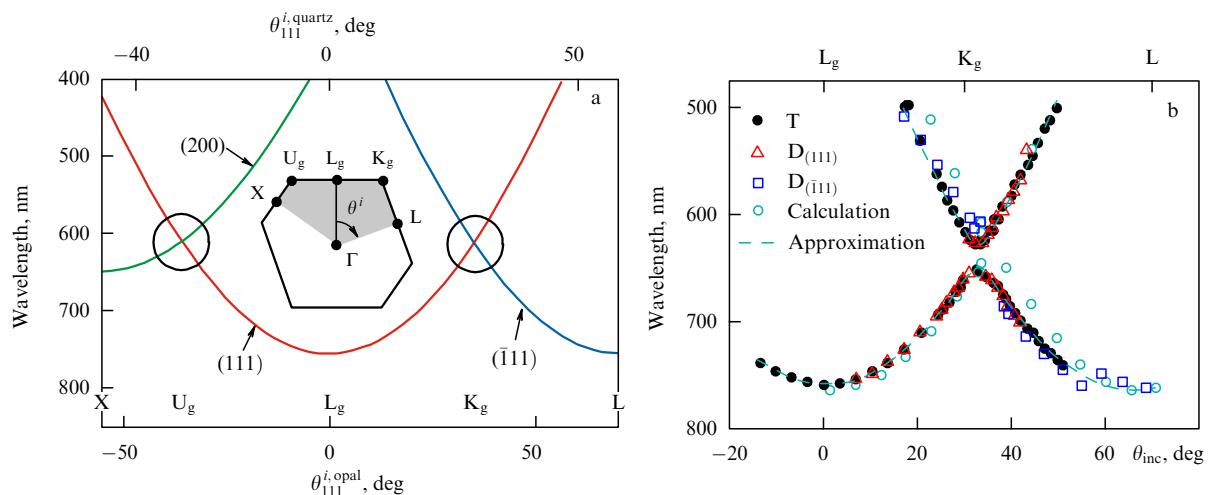

Figure 2. (a) Bragg wavelengths in opals calculated by neglecting the anticrossing effect. The symmetry points of the first Brillouin zone surface are shown on the lower axis. The corresponding angles of incidence on the opal film calculated by Snell's law are presented on the upper axis. Points corresponding to the MBD regions are indicated by circles. The inset shows the section of the Brillouin zone of the fcc lattice corresponding to the experiment. (b) Results of experimental MBD study in opals. Positions of transmission (T) and diffraction (D_{111} and $D_{\bar{1}11}$) bands corresponding to the (111) and ($\bar{1}11$) photonic stop-bands and Bragg approximation of experimental data phenomenologically taking into account the interaction of light beams in the MBD region [41].

and the basic optical properties are determined by extended Bragg resonances of the crystal lattice.

Among the numerous different periodic PC structures, we will accentuate a close-packed face-centered cubic (fcc) lattice consisting of spherical particles, which exists in PCs in the direct [34] (Fig. 1a) and inverted [42] variants. Photonic crystals formed by spherical particles of amorphous silicon dioxide a-SiO$_2$ (natural and synthetic opals) [43–45], TiO$_2$ [46], and various colloidal materials [36, 47, 48] were investigated in detail. Figure 1b presents the Brillouin zone of an fcc lattice and Fig. 1c shows the photonic band diagram of a PC formed by polystyrene spheres ($n_{\mathrm{eff}} \approx 1.4$ at 2.5 μm) [35]. The transmission spectra of low-contrast opal-like PCs exhibit relatively narrow resonance lines related to Bragg reflection of light from (hkl) plane systems, i.e., with (hkl) photonic stop-bands. The (111) Bragg resonance has the

lowest frequency and, as a rule, the maximum intensity. The energy position of the (111) stop-band is shown by a circle in Fig. 1c. Figures 1d, e show the dependence of parameters of the (111) Bragg reflection peak on the number of layers in the [111] direction for a polystyrene PC [36]. One can see that the photonic stop-band is formed at a sample thickness of about 20 layers.

At Brillouin zone singularities, multiple Bragg diffraction (MBD) [41, 47, 49–52] can be observed which appears with the simultaneous coincidence of frequencies and wave vectors of two or more photon dispersion curves, resulting in the anticrossing (repulsion) of dispersion branches (region denoted by the dashed circle in Fig. 1c). Figure 2a demonstrates two MBD regions inside the circles. The multiple Bragg diffraction corresponding to the K point in the Brillouin zone is observed due to the crossing (in the case
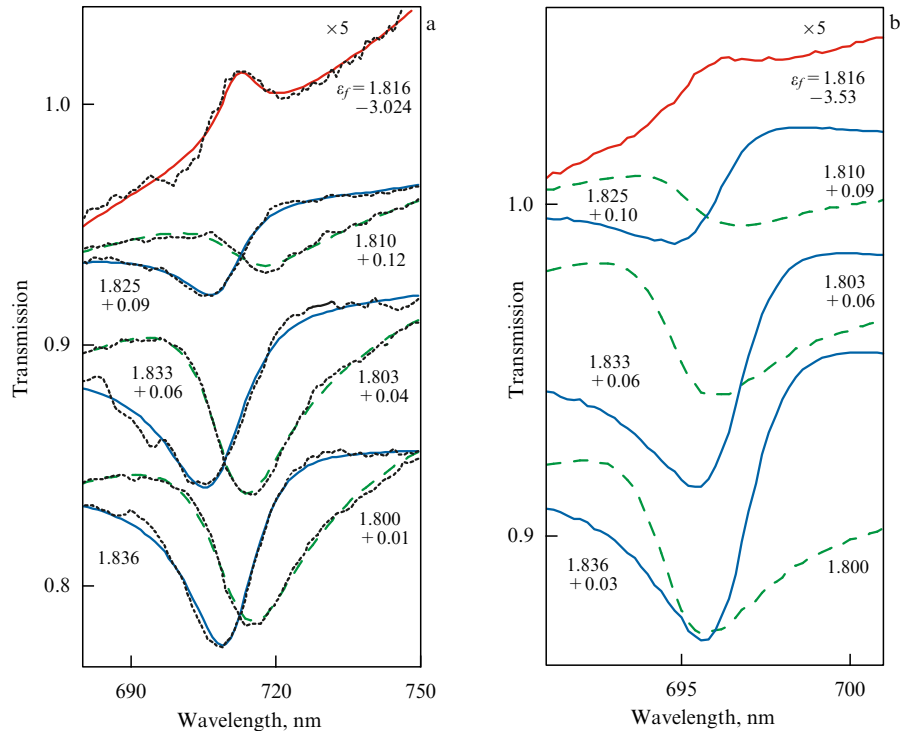
Figure 3. (Color online.) Fano resonance in the transmission spectra of an opal–filler PC for different permittivities ε_f of the filler. (a) Black curves are the transmission spectra of a 0.6-mm-thick sample ($D = 316$ nm) in the region of the (111) Bragg line. Color curves approximate experimental spectra using the Fano formula. (b) Calculated transmission spectra of an unordered opal–filler PC. The vertical shift of spectra in Figs 3a, b is indicted at each spectrum together with the value of ε_f (from Ref. [53]).

of a negligibly low contrast) of dispersion curves corresponding to the (111) and ($\bar{1}$11) planes, while MBD at the U point is observed due to the crossing of dispersion curves corresponding to the (111) and (200) planes. Already in the case of a very low contrast corresponding to opals, the repulsion of dispersion curves is experimentally observed in the MBD region in both transmission and reflection spectra (Fig. 2b) [41].

2.2 Resonances in photonic structures with different disorder types

We will now proceed from perfectly ordered structures to real structures with inherent inner disorder and to structures with artificially produced defects. In all these cases, new scattering channels, which can have a pronounced resonance character, are manifested in the spectra.

We will demonstrate these phenomena by the example of opals. Structural studies have demonstrated the twinning of the fcc opal lattice along the [111] growth axis and also revealed two fluctuating parameters of a-SiO$_2$ spheres themselves: the particle size and shape slightly changed from particle to particle (variation in the diameter was within 7% [53]) as did permittivity [56, 57]. The variation in the permittivity related to the inhomogeneous structure of a-SiO$_2$ particles leads to fluctuations in light scattering from each of the particles, resulting in the appearance of a broad uncompensated scattering component. The interference of the waves corresponding to a broadband scattering component and a narrow Bragg line is the classical condition for the appearance of the well-known Fano resonance [58–60] with the asymmetric profile described by the expression [61, 62]

$$\sigma(\Omega) = D^2 \frac{(q + \Omega)^2}{1 + \Omega^2}, \qquad (1)$$

where $q = \cot \delta$ is the Fano parameter, δ is the phase difference between a discrete state and a state in a continuum, $D^2 = 4 \sin^2 \delta$, $\Omega = 2(\omega - \omega_0)/\Gamma$ is the dimensionless frequency, and parameters Γ and ω_0 are the decay and frequency of the narrow line, respectively. The Fano parameter q in opals characterizing the (111) Bragg band shape in transmission spectra is related to the contrast between the permittivity of a filler and the permittivity determined by the opal structure. In the case of zero contrast ($\varepsilon_f = 1.816$, $q = 0$), a Bragg transmission peak appears in the spectrum instead of the Bragg reflection band traditionally observed (Fig. 3). Note that the study of 1D disordered photonic structures has shown that the dimension disorder (the structural element length disorder) leads only to the broadening and degradation of Bragg resonances, whereas the permittivity disorder gives rise to the Fano resonance and the flip of Bragg bands in transmission spectra [63].

Original optical materials are photonic glasses — disordered structures formed by monodisperse polymer microspheres from 200 nm to a few micrometers in diameter with a polydispersity of less than 2% (see the inset in Fig. 4) [54]. This disordered material represents solid films with a number of nontrivial properties due to the resonance Mie scattering from the dielectric spheres forming them. While the optical properties of ordered (although not perfect) PCs, like opals, are determined by extended Bragg resonances, in a photonic glass, local resonances play a leading role. These resonances are observed in transmission spectra as a sequence of lines whose positions are determined by the diameter d of spheres and the refractive index n (Fig. 4).

Periodic structures in which the dielectric response of one of the forming elements as a function of frequency has a pole at some Bragg resonance frequency were separated into a special class of resonance PCs [64, 65]. The simplest model of
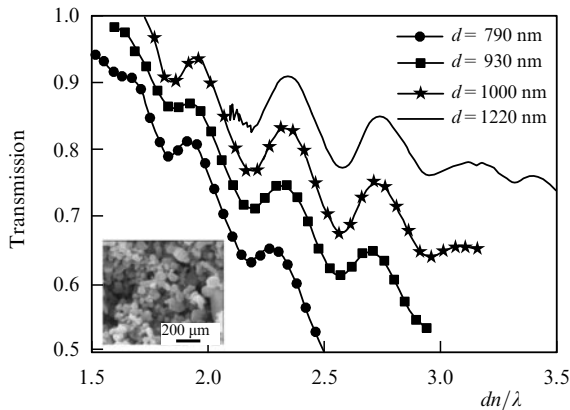
Figure 4. Normalized diffuse transmission of white light through photonic glasses as a function of the parameter dn/λ. The scale corresponds to the spectral range from 500 to 920 nm. Samples consist of spheres with four different diameters d; the thickness of each sample is about 100 μm. The inset shows an SEM image of a photonic glass (adapted from [54]).

a resonance PC assumes that the points of a periodic lattice contain two-level systems with the transition frequency ω_0 and the nonradiative excited-level decay Γ. For a small number N of resonance layers, the intensity and half-width of the reflection band monotonically increase with increasing N. As N is further increased, a passage to the PC regime is observed in which the half-width of the reflection band is saturated forming a Bragg photonic stop-band.

Among the resonance Bragg systems, of special interest are nonperiodic structures with long-range order, in particular, Fibonacci structures (Fig. 5a) [55, 66–69]. The Fibonacci structure, whose spectra are presented in Fig. 5b, was formed by 21 quantum wells with the thickness 22 nm grown between 5-nm-thick $Al_{0.3}Ga_{0.7}As$ barriers. The length of layers A and B required for preparation of the resonance Bragg Fibonacci structure was achieved by adding intermediate $Al_{0.04}Ga_{0.96}As$ layers, so that the thickness of layers A and B was about 82 and 134 nm, respectively [55].

Figure 5 presents the spectra of structures in which the interval between quantum wells corresponds to the Fibonacci

sequence (Fig. 5b) and does not correspond to (Fig. 5c), being equidistant. One can see that reflection bands (stop-bands) are quite smooth in the case of a periodic structure and have the superstructure for samples with the Fibonacci sequence. In these spectra, the superstructure is observed for the exciton resonance of both heavy holes (HHs) and light holes (LHs). The strongest effect is observed for the exactly coinciding parameters $d/d_{Bragg} = 1$, where d is the structure period and $d_{Bragg} = \lambda_0/(2n)$.

2.3 Resonance effects
related to photonic crystal boundaries
Another example of resonance phenomena is the observation of the optical analog of Tamm states in the transmission spectra of magnetophotonic crystals [70]. The interference resonance related to excitation of a Tamm state is localized at the interface of two 1D photonic structures, each of them containing five Bragg mirror layers: SiO_2/Ta_2O_5 in the left half of the sample and $SiO_2/Bi:YIG$ on its right side (Bi:YIG is a bismuth-doped yttrium garnet) (Fig. 6a). Bragg mirrors maintain the optical Tamm state, which was experimentally observed as a narrow resonance at a wavelength of 800 nm inside a broad forbidden band (Fig. 6b). At the same wavelength, an increase in the Faraday rotation angle was observed, in contrast to that in an unstructured magnetooptic material (Fig. 6c).

Thus, the magnetic response in a 1D magnetophotonic crystal increases due to localization of an electromagnetic wave, i.e., the implementation of the multipass regime for resonance modes inside Bi:YIG layers. This results in summation of the polarization-plane rotation after each passage of the wave, leading to large Faraday rotation angles per optical path unit in the structure. Note that surface states in PCs were considered in review [71].

2.4 Bound states in the continuum
in photonic-crystal membranes
Resonance effects in photonic-crystal membranes have been described in the literature in detail. These membranes represent profiled thin plates made of high-index materials
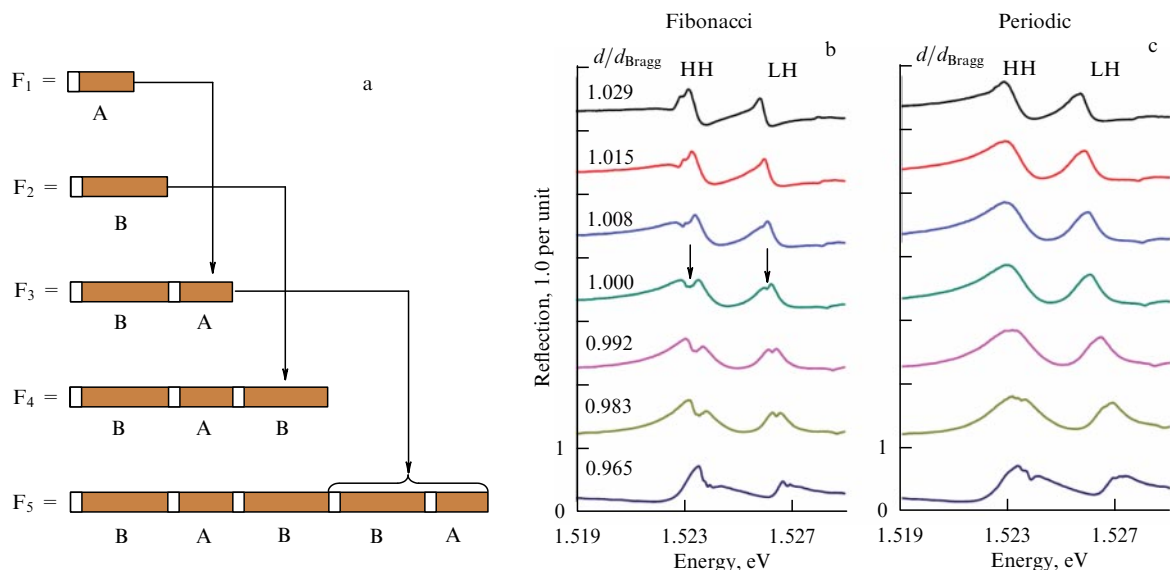

Figure 5. (a) Formation algorithm of a Fibonacci structure with quantum wells. (b, c) Experimental reflection spectra for different d/d_{Bragg}. The interval between quantum wells in Fig. 5b corresponds to the Fibonacci sequence, in Fig. 5c to the equidistant interval $\lambda_0/2$ (data from [55]).
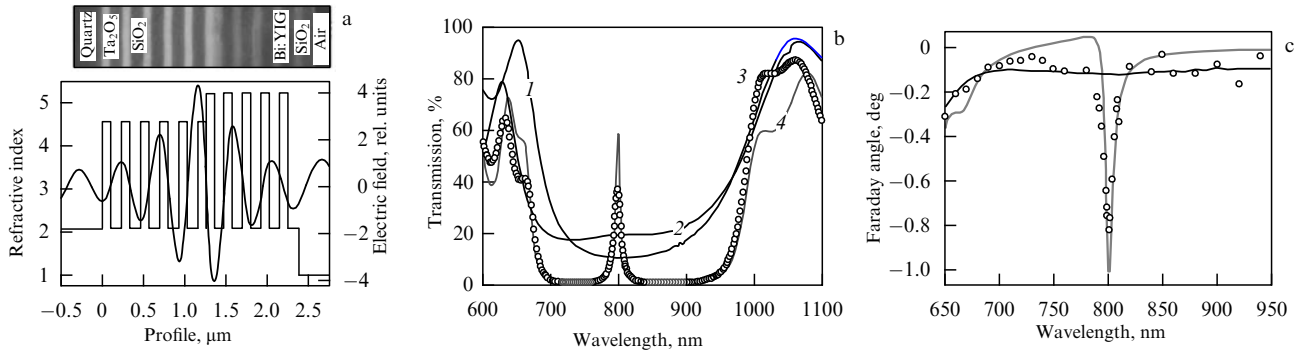
Figure 6. (a) Permittivity distribution for a one-dimensional magnetophotonic crystal and the calculated electric field distribution at the resonance frequency. The inset shows the SEM image of the sample. (b) Transmission spectra of a nonmagnetic (curve *1*) and magnetic (curve *2*) PC. Transmission spectra of a one-dimensional magnetophotonic PC consisting of two PCs (curve *3*) and calculated spectrum (curve *4*). (c) Faraday rotation spectrum: reference $(SiO_2/Bi:YIG)_5$ structure (black curve), one-dimensional magnetophotonic crystal: experiment (circles) and calculation (grey curve) (adapted figure from [70]).

(as a rule, silicon) surrounded by air from the top and bottom. Such membranes can be treated both as waveguides providing light propagation in the normal direction due to total internal reflection and as 2D PCs controlling the light wave in the two remaining directions [37, 38, 72]. Photonic-crystal membranes exhibit resonance states with very long lifetimes (tending theoretically to infinity) — so-called bound states in the continuum (BICs) [73, 74].

Note that BICs were theoretically predicted at the dawn of the development of quantum mechanics as states with energies above zero (the potential value in the remote spatial region), i.e., located in the continuum of free states, but remaining near some potential for an arbitrarily long time [75].

In the electrodynamic problem, all the photons have positive energy and a photon cannot be bound in a potential well [38]. Therefore, the problem of the existence of BICs for electromagnetic waves attracts great interest. Note that several photonic BIC formation mechanisms exist. The most known mechanism is determined by the mode symmetry. If an odd mode with a zero wave vector can exist in a membrane, this mode cannot be coupled to free-space modes, because they are even states [76]. In addition, the realization exits described by Friedrich and Wintgen for the electron problem [77]. If two modes exist which are mutually orthogonal inside the system and are coupled to each other only via the surrounding space, these modes are hybridized, so that the leaking 'tails' of one mode will interfere constructively, whereas the 'tails' of another mode will interfere destructively, quenching each other. As a result, the second mode is a BIC in the ideal case.

To observe a BIC, some parameter is usually varied (for example, the angle of wave incidence on a sample), and the resonance line quality (Q) factor is traced. Let p be the parameter value, and $p = p_0$ is the BIC appearance condition. Then, the resonance state comes to behave unusually in some vicinity $|p - p_0| < \delta_{BIC}$. As the parameter approaches the BIC condition $p = p_0$, the resonance linewidth tends to zero and the spectral singularity disappears [73]. As the parameter further changes, the spectral linewidth increases again. Thus, the Q factor demonstrates in the interval $|p - p_0| < \delta_{BIC}$ the characteristic $Q \propto |p - p_0|^{-\alpha}$ 'resonance' dependence, where α is a positive number depending on the BIC type.

Note that BICs cannot exist in real systems; however, so-called supercavity modes with a finite lifetime can appear [78].

It is important to emphasize that supercavity modes are not resonances with an extremely high Q factor, but are modes appearing through a mechanism corresponding to the BIC appearing mechanism. The Q factor in the vicinity $|p - p_0| < \delta_{sc}$ of the supercavity mode also demonstrates the 'resonance' dependence, but does not tend to infinity, remaining limited by some saturation value $Q < Q_{max}$ [78]. Such a characteristic 'resonance' dependence of the Q factor in the vicinity of the supercavity mode allows one to distinguish it from usual resonance states for which changes in the system parameters do not result in the appearance of pronounced Q factor maxima. High-Q supercavity modes can be used to enhance nonlinear effects [79] and produce lasing [80].

3. Resonance structural elements

3.1 Optical antennas

The advent of MMs is historically related to the simulation of processes in a plasma with an effective permittivity ε_{eff} with the help of metal wires [5] and also to paper [6] describing a medium with an effective magnetic susceptibility μ_{eff} prepared with the help of ring resonators. The structural elements of such materials long known in radiophysics are used as antennas or their constituent elements [84].

Problems with decreasing the operating wavelength of MMs on passing to micro- and nanooptoelectronic devices are related not only to the miniaturization of structural elements but also to the different behavior of metals in different spectral ranges. Studies of optical responses of structural elements of MMs resulted in the development of a new field in photonics called optical antennas [85–87]. Unlike the structural elements of MMs, optical antennas are used to transform electromagnetic waves from the far wave zone to near fields and vice versa.

Initially, nanoantennas were made of elongated metal elements (resembling elements of radio antennas) (Figs 7a–d) in which a plasmon resonance appears [81, 88, 89]. The efficient localization of the electric field due to a plasmon resonance appears near acute angles (Figs 7e, f). For this reason, triangular elements are also used as metal antennas [82, 90, 91]. Such antennas allow one to extract efficiently light from nanosources or detect the harmonic generation at lower pump intensities.
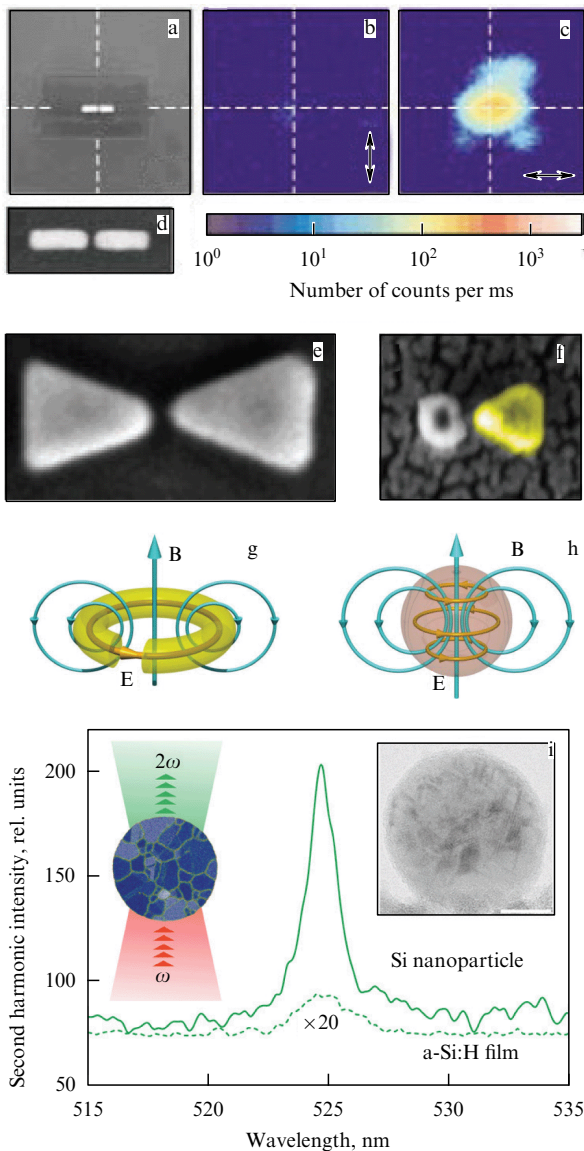
Figure 7. (Color online.) (a) Image of a resonance half-wave gold nanoantenna. Generation of light by the nanoantenna excited by laser pulses polarized across (b) and along (c) the antenna. The image area in Figs a–c is 2 × 2 µm. (d) Magnified image of the antenna shown in Fig. 7a; the image area is 450 × 180 nm. (e) Gold 'bowtie'-type nanoantenna image. (f) Image of a triangle gold nanoantenna (yellow color) modifying the scattering spectrum of a palladium nanoparticle for detecting hydrogen. Schematic distributions of the electric and magnetic fields produced by elements with a magnetic response: (g) a split-ring resonator and (h) a spherical particle with high permittivity. (i) Second harmonic generation spectrum of a silicon nanoparticle (solid curve) compared to that of an a-Si:H film (dashed curve). The left side of Fig. 7i shows the schematic diagram of the experiment; the inset in the right part shows a transmission electron microscopy image of a granulated nanoparticle. (Figures 7a–d are adapted figures from [81], Fig. 7e is taken from [5], Fig. 7f is adapted from [82], Figs g, h are from [23], and Fig. 7i is adapted from [83].)

In 2012, it was proposed to use weakly absorbing dielectric particles with a high refractive index as nanoantennas [28]. These particles have magnetic Mie resonances along with electric resonances. Magnetic Mie modes appear due to 'twisted' displacement currents inside a spherical particle, producing a secondary magnetic field in the transverse direction (Figs 7g, h). Silicon is often used as a high-refractive index material in many studies. Although silicon is

a centrally symmetric material, it was found that efficient second harmonic generation could be observed in silicon antennas. The efficient second harmonic generation in nanoparticles prepared by laser ablation was demonstrated experimentally and theoretically in [83]. The effect is related to the granular structure of these nanocrystal particles (Fig. 7i). The 525-nm green light generation efficiency for silicon nanoparticles is two orders of magnitude greater than that for nonstructured silicon films (Fig. 7i). This result was achieved due to optimization of the subcrystal (granules) and crystal (size) parameters of nanoparticles maintaining magnetic dipole Mie resonances.

The individual elements of antennas are grouped in clusters to increase the efficiency [95–97] and to form a directional pattern [98]. In radio physics, Yagi–Uda antennae are well known, consisting of a reflector suppressing radiation in the direction of this element and also of one or a few directors redistributing the directional pattern in a different direction [99]. For the optical range, Yagi–Uda antennas based on metal structural elements [100–102] and spherical silicon particles [103, 104] have been proposed. It was shown in [105] that the formation of the directional pattern in Yagi–Uda antennas can be interpreted in the Fano resonance model. The resonance frequency of the larger-size reflector is lower than the radiation frequency of a nano-object. As a result, the reflector reemits the field in the opposite phase, resulting in the destructive interference of radiation in the reflector direction. The smaller-size director has a higher resonance frequency and therefore reemits in-phase with the source.

3.2 Fano resonances in homogeneous dielectric particles

Interesting effects are also observed in single dielectric particles. Because of a large set of resonance states, an interference interaction between them takes place, giving rise to Fano resonances in scattering spectra [60]. Thus, in papers [106, 107], devoted to Mie scattering by spherical particles, Fano resonance was discovered, which appeared due to the interaction of a dipole resonance (broad band) with a quadrupole resonance (narrow band). As shown numerically [92, 108] and analytically [93], in the case of a high refractive index, the resonance Mie scattering in dielectric spherical particles and cylinders can be described as cascades of Fano resonances.

Figure 8a shows spectra of the integral Mie cross section $Q_{\text{sca}, 0}$ of scattering by an infinite homogeneous cylinder for dipole TE_{0k} modes as functions of the permittivity ε. The scalability of Maxwell's equations allows us to present spectra as functions of a dimensionless quantity proportional to frequency, which is called the size parameter in the Mie theory: $x = kr = 2\pi r/\lambda$, where k is the wave number, r is the particle radius, and λ is the wavelength in a vacuum.

In order to make sure that the Mie scattering spectra consist of cascades of Fano resonances, contours of the resonance TE_{nk} lines were approximated by expression (1) and the Fano parameter q was determined for each line. The profiles of 900 resonance lines ($1 \leqslant k \leqslant 9$, $\varepsilon = 1 - 100$ with the step $\Delta\varepsilon = 1$) were used in calculations. Sets of q values were obtained which form, in fact, continuous curves exactly corresponding to the dependence $q(x) \propto \cot x$ in Fano expression (1). The inset in Fig. 8a shows dependences $q(x)$ for the dipole TE_{0k} mode and multipole TE_{1k} and TE_{2k} modes [92]. Similar dependences for $q(x)$ were obtained in [93] analytically for a dielectric sphere (Fig. 8b) and a cylinder.
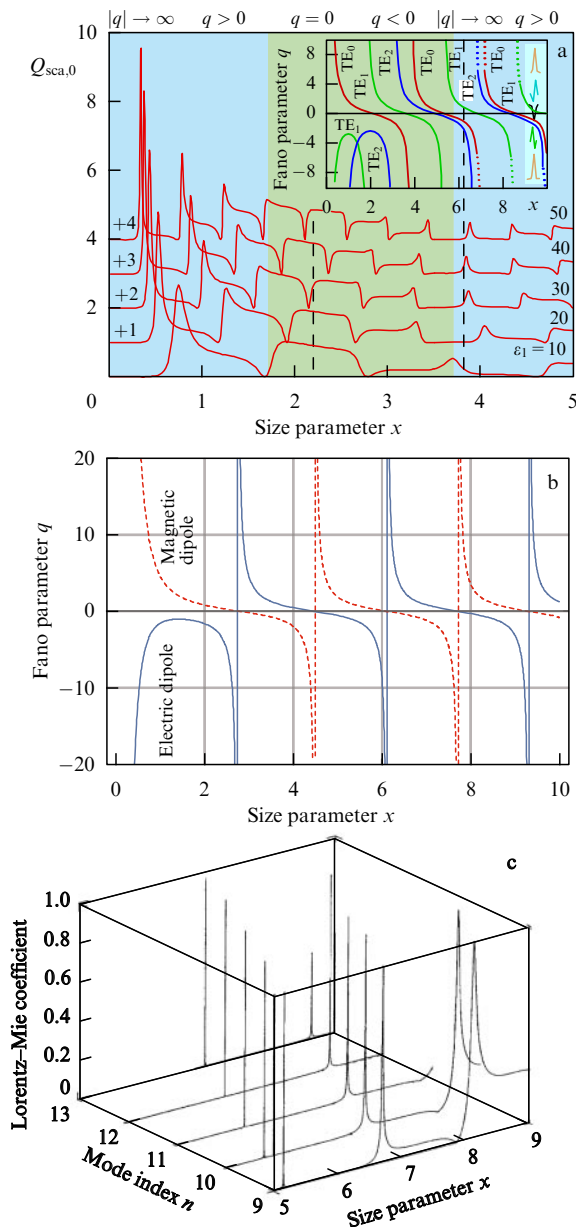
Figure 8. (Color online.) (a) Spectra of the integral cross section $Q_{sca,0}$ for the dipole TE_{0k} mode for Mie scattering by a homogeneous cylinder as functions of ε in the normalized frequency scale $x = 2\pi r/\lambda$; the inset shows Fano parameters $q(x)$ for the TE_{0k}, TE_{1k}, and TE_{2k} modes. (b) Dependences $q(x)$ analytically calculated for a homogeneous dielectric sphere for electric dipole modes (blue solid curves) and magnetic dipole modes (red dashed curves). (c) Lorentz–Mie coefficients for electric moments of a microsphere ($\varepsilon = 6$) corresponding to whispering-gallery modes (modes with large values n of the orbital moment). Figure 8a is adapted from [92], Fig. 8b from [93], Fig. 8c from [94].

Note that spectra resembling in shape cascades of Mie resonances were obtained in calculations of the interaction of a two-level atom with electromagnetic modes of a dielectric microsphere (whispering-gallery modes) (Fig. 8a) [94]. Fano resonances were also recently observed in scattering by cylinders surrounded by a uniaxial hyperbolic medium [109].

3.3 Invisibility regimes of resonance particles
In recent years, constantly increasing interest in metamaterials has initiated the development of a new field of research

concerning the invisibility and cloaking of material objects [15, 110, 111]. The results of these papers have become to some extent the implementation of a favorite idea of science-fiction writers about a cloak of invisibility.

Invisibility in the regime of interference quenching of scattering for objects in shells was realized, notably, based on nonlinear effects in multilayer structures [112] using graphene coatings [113] and also in the magnetooptical effect regime induced by an external magnetic field [114]. However, in high-contrast dielectric cylindrical particles, an invisibility regime can be achieved even without using masking shells due to the resonance Mie scattering described by a cascade of Fano resonances. It is known that the Fano contour intensity vanishes (for $q = -\Omega$ in (1)) because of the destructive interference of two waves. Thus, by combining resonance and nonresonance scattering, we can produce conditions for the invisibility of a single particle due to interference quenching of the scattering intensity at the frequency of the Fano contour minimum [16, 115, 116].

3.4 Supercavity modes
in subwavelength dielectric cylinders
The existence of supercavity modes in subwavelength dielectric cylinders was theoretically demonstrated in 2017 [117]. Recall that supercavity modes (which were discussed in Section 2.4) are formed similarly to the appearance of bound states in the continuum.

In finite dielectric cylinders, two mechanisms of electromagnetic mode formation can be distinguished. The first is the Mie modes related to the circular profile of the cylinder. The second is the Fabry–Perot modes appearing between two flat boundaries at the cylinder ends. As the cylinder height l is changed, its radius r being invariable, the Mie mode frequency will change negligibly, unlike Fabry–Perot modes (Fig. 9). For certain r/l aspect ratios, the anticrossing region related to the formation of a hybrid state is observed (Fig. 9b). In this case, modes inside the cylinder remain orthogonal and coupling is performed via the surrounding space, corresponding to the Friedrich–Wintgen mechanism [77] discussed in Section 2.4 for photonic-crystal membranes. In dielectric cylinders, the 'resonance' increase in the Q factor is observed when the optimal value of the parameter r/l is achieved, which is typical for supercavity modes. Then, the mode Q factor again returns to the characteristic value for noninteracting resonances (Fig. 9d).

Figure 9 shows the formation of a supercavity mode in a dielectric cylinder with $\varepsilon = 80$ due to hybridization of the TE_{020} (quasi-Mie) and TE_{012} (quasi-Fabry–Perot) modes. On coordinate axes, the dimensionless quantities, including the size parameter $x = 2\pi r/\lambda$, are plotted. Thus, the supercavity mode frequency can be determined from the specified size of a sample and, vice versa, the required size of a sample can be determined from the specified frequency. The Q factor of the TE_{020} and TE_{012} modes outside the hybridization region are of the order of 10^2 [118]. The optimal value $r/l = 0.703$ corresponds to the supercavity mode with $Q \approx 6.5 \times 10^4$, which is two orders of magnitude higher than the Q factors of the TE_{020} (quasi-Mie) and TE_{012} (quasi-Fabry–Perot) resonances of the cylinder outside the interaction region. Such a supercavity mode can be used for the efficient localization of the electromagnetic energy in a subwavelength volume. The use of supercavity modes to increase the second harmonic generation efficiency was proposed in theoretical paper [119].
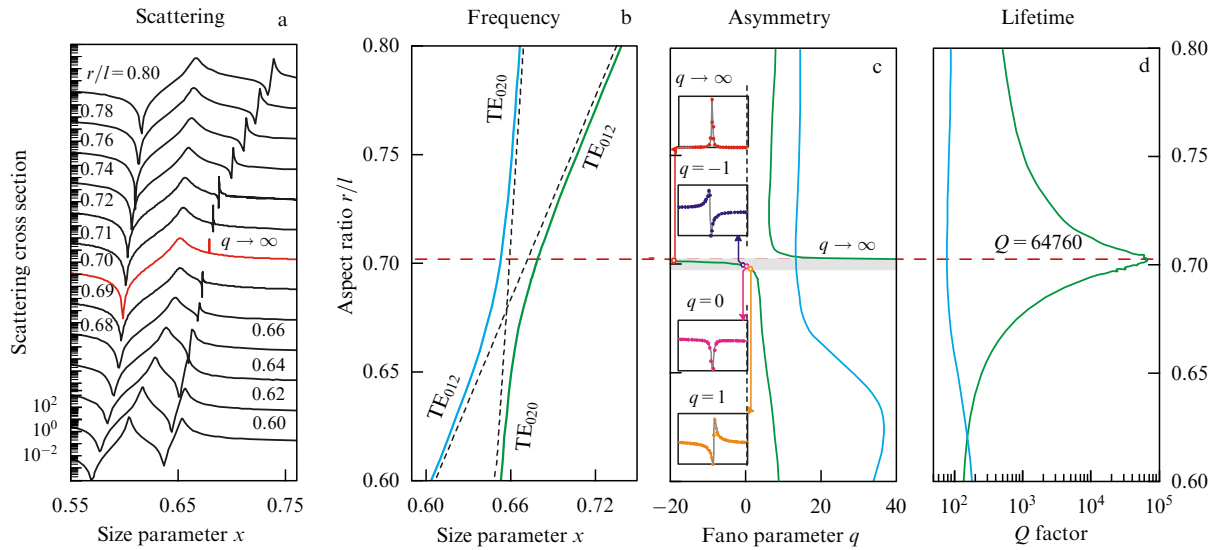
Figure 9. (Color online). Analysis of the TE_{020} (quasi-Mie) and TE_{012} (quasi-Fabry–Perot) photon modes in the anti-crossing region. (a) Scattering spectra of a TE polarized plane wave (magnetic field oscillates along the z axis, then the wave vector is perpendicular to the z axis) scattered by a cylinder ($\varepsilon = 80$) as functions of the parameter r/l. The supercavity mode appears for $r/l = 0.703$ (red spectrum). Spectra are displaced from each other by 100 dB. (b) Frequencies of the TE_{020} and TE_{012} modes. (c) Fano parameter for both modes. Insets show the high-frequency spectral features at a linear scale for values in a narrow interval of r/l indicated by different colors ($r/l = 0.698$, $q = 1$; $r/l = 0.699$, $q = 0$; $r/l = 0.700$, $q = -1$; $r/l = 0.703$, $q \rightarrow \infty$). (d) Q factor demonstrating the dependence typical for a supercavity with the maximal value close to $Q = 65,000$. Data in Figs 9b–d are obtained by the approximation of spectral lines by Fano formula (1). Blue and green curves correspond to the low- and high-frequency branches [117].

In [120], distilled water was used as a high-refractive index material with the room-temperature permittivity $\varepsilon \approx 80$ in the frequency range from 1 to 6 GHz [121]. The measured scattering spectra exhibited the region of antic-rossing of the TE_{110} (quasi-Mie) and TM_{111} (quasi-Fabry–Perot) modes. However, large material losses in water in the microwave range prevented the formation of a high-Q bound state in this region. The problem of losses can be solved, for example, by using weakly absorbing ceramic materials. We anticipate the appearance of experimental papers confirming the existence of supercavity modes in dielectric resonators.

4. Metamaterials

4.1 Three-dimensional metamaterials
The magnetic permeability in usual materials at optical frequencies is known to be close to unity [123], unlike the permittivity which in natural materials can take values from $\varepsilon \approx -15$ in metals [124] to $\varepsilon \approx 15$ in semiconductors [125].

Veselago considered the features of solving the electro-dynamic problem with the help of a $\varepsilon-\mu$ diagram [11] in which both variables can take both positive and negative values (Fig. 10). The usual solutions of Maxwell's equations correspond to the first quadrant ($\varepsilon > 0$, $\mu > 0$). Evanescent exponentially decaying waves correspond to the second ($\varepsilon < 0$, $\mu > 0$) and fourth ($\varepsilon > 0$, $\mu < 0$) quadrants. The author of [11] focuses on the third quadrant ($\varepsilon < 0$, $\mu < 0$), because vectors $\mathbf{E}$, $\mathbf{H}$, and $\mathbf{k}$ of a plane wave in such media form a left-hand triple and the refractive index takes negative values. In such 'left-handed' media, the phase and group velocities have opposite directions and an inversion of the Doppler and Vavilov effects should be observed. Veselago's paper [11] has laid the foundations of a new direction in the creation of objects with the most unusual properties, for example, a plane lens made of a left-handed material.
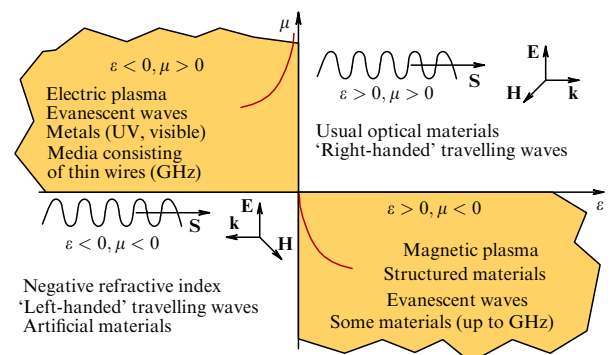

Figure 10. Diagram classifying materials by their permittivity and magnetic permeability. Quadrants 1 and 3: wavy curves show the field amplitude in materials where travelling waves propagate ($\mathbf{S}$ is the Umov–Poynting vector); arrows show the $\mathbf{E}$, $\mathbf{H}$, $\mathbf{k}$ vector triples. Quadrants 2 and 4: the red exponential curve corresponds to the field amplitude in materials where evanescent waves exponentially decay with distance (adapted from [122]).

Nevertheless, the results of Ref. [11] were considered for a long time only to be purely speculative, having nothing in common with the real world.

As pointed out in the Introduction, in the 1990s, Pendry studied the formation of a plasma, simulating processes in the microwave range with the help of artificial media consisting of subwavelength resonance elements [5]. The understanding of the possibility of creating an artificial medium with effective magnetic susceptibility has become a real revolution [6]. Such media were later called 'metamaterials' [22]. In pioneering MM studies, these objects were defined as artificial media with effective parameters whose nature is related to the resonance response of structural elements to electric and magnetic fields [22, 126]. It is important to note that a definition of effective parameters is possible due to the homogenization procedure in a spectral region where the

wavelength significantly exceeds the characteristic size of the MM lattice constant.

Later, MMs were used to demonstrate experimentally negative refraction in prisms [23, 127], and the plane lenses proposed by Veselago [13] were also implemented. Along with MMs made of metal components like split-ring resonators, objects with nontrivial properties were created based on dielectric structural elements in which magnetic Mie resonances can be excited [27].

It is useful to compare the sizes of dielectric particles normalized to the wavelength with the normalized sizes of split-ring resonators. The Mie resonance of silicon particles 160 nm in diameter corresponds to a wavelength of 720 nm [128], i.e., the wavelength is 4.5 times larger than the dielectric particle diameter. For comparison, double metal split-ring resonators used in [22] were 3.3 mm in size at the resonance wavelength of 62 mm, i.e., the ring resonator size was 19 times smaller than the wavelength. Thus, dielectric structural elements have larger normalized sizes than do metal resonators, but such structures can be prototyped in the entire spectral range. Also, dielectric materials usually weakly absorb, whereas metal structural elements have high ohmic losses. The compensation of losses with the help of an amplifying medium is considered in the review [129].

The advent of MMs gave a considerable impetus to the development of the homogenization theory describing a complex structure with the help of effective parameters [130]. The homogenization theory describes the passage from exact solutions of the electromagnetic problem (microscopic description) to averaged fields extended over a continuous medium. The most important for practical applications and at the same time the most complicated homogenization problem is boundary conditions [131]. The derivation of boundary Maxwell conditions assumes the homogeneity of the medium at arbitrarily small distances from the interface of two media, which obviously does not correspond to the case of artificial materials [132]. As a result, the use of effective material parameters in calculations leads to some deviations from the exact solution. Such deviations can be eliminated by introducing, for example, an additional surface layer with certain material parameters [132].

The preparation of materials with the specified distributions $\varepsilon(\mathbf{r})$ and $\mu(\mathbf{r})$ provided by properly arranged resonance structural elements opens up broad opportunities for controlling electromagnetic waves. According to the variational Fermat principle, light propagates between two points along the minimal optical path [133]. A well-known example: a change in the refractive index of air caused by inhomogeneous temperature distribution can give rise to mirages. For an arbitrary space, an optical metric tensor depending on the refractive index can be introduced [134]. By transforming coordinates, the tensor can be changed to obtain a simple solution to a problem with a new distribution of the refractive index. The field of optics using such transformations for solving electrodynamic problems is called 'transformation optics' [15, 110, 111, 135].

The most important result of transformation optics is the determination of the distribution of material parameters ε and μ (usually anisotropic) used for creating masking coatings [136]. A homogeneous space is transformed to 'expand' a microscopic region, from which scattering can be neglected, into a macroscopic volume. In this case, parameters ε and μ in the transformed space will depend on the coordinates. As a result, a light wave propagating almost without scattering in

the initial space will also propagate without scattering in the transformed space bypassing the macroscopic region, which becomes invisible. It is known that it is impossible to make an object completely invisible; however, this does not prevent the suppression of scattering to a negligible value [137–139]. In the given case, the propagation of a light wave through a macroscopic object will be accompanied by a weak scattering component observed in the transformed space, which is identical to scattering by a microscopic object in the initial space before the transformation.

To create a masking coating, it is necessary to specify the required spatial distribution of ε and μ, which can be achieved by using resonance structural elements [140]. In experimental studies, the elements with magnetic and electric responses based on split-ring resonators [141], spirals [142], and dielectric particles with Mie resonances were used [143].

Note that, aside from invisibility, a mathematical apparatus of transformation optics is used for the relatively simple description of scattering by plasmon particles [147]. The methods of transformation optics are also used in cosmology. In [148], a method of experimental simulations of the gravitational curvature of space near massive space bodies under laboratory conditions was proposed. The method uses materials with a spatially-dependent optical metric tensor.

4.2 Metasurfaces

The creation of 3D MMs is a complicated technological problem. Note that in MMs with a negative permeability, an electromagnetic wave decays in fact in the first layer of the structural elements. Because of this, metasurfaces consisting of an ordered set of resonance elements located in one plane (for example, on a substrate) are becoming widespread at present [25, 26, 87, 149]. Standard optical elements such as lenses, quarter-wavelength plates, and plates with recorded holograms perform their functions due to a continuous change in the wave front during the propagation of radiation over distances considerably exceeding the wavelength. Thus, significant changes in the amplitude, phase, or polarization of light waves are gradually accumulated along the optical path.

By using metasurfaces consisting of a layer of scattering resonators, it is possible to create plane optical elements modifying the wave front at subwavelength distances. It is known that the response phase changes by π after propagation through the resonance frequency. As a result, individual resonators having a certain response to the incident electromagnetic wave with the specified frequency, according to Huygens's principle, form a wave front with the required characteristics.

For example, Fig. 11a shows a metasurface cell consisting of eight V-shaped resonance scatterers [144] constructed so that the phase shift of an IR wave increases by $\pi/4$ from element to element. As a result, the phase of the scattered wave in the cell runs 2π, and the propagating beam is deviated from the normal with the help of a plane device (Fig. 11b).

Metasurfaces also can be used to generate beams with optical vortices. In [145], a Huygens metasurface was demonstrated (forming forward scattering), which consisted of silicon nanodiscs located in the points of a square lattice. The metasurface was divided into four quadrants that differed in lattice constants changing coupling parameters between resonances in scatterers, resulting in a change to the phase of the propagating field. A Gaussian beam propagated through such a metasurface transforms into a beam with the
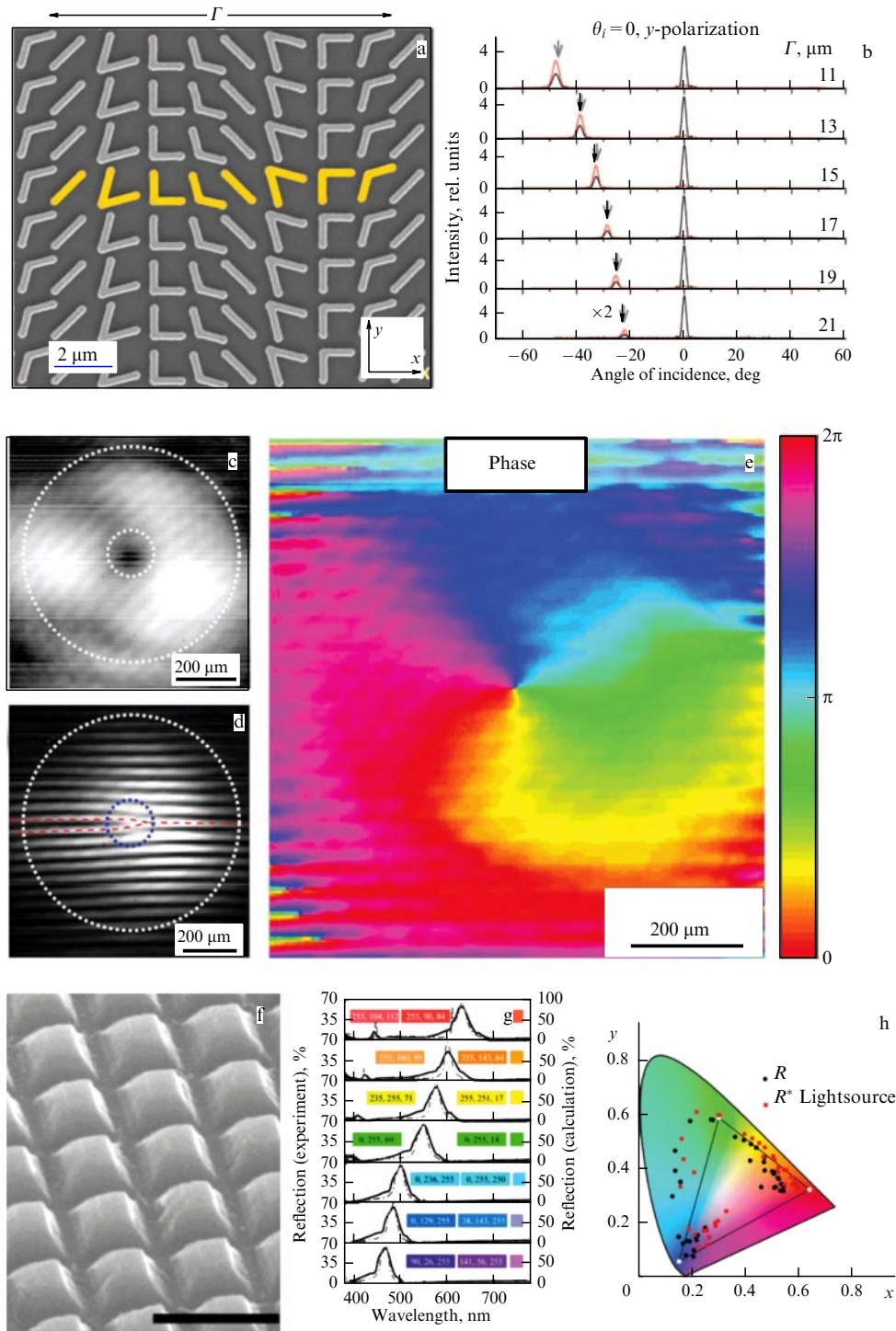
Figure 11. (Color online.) (a) Image of a deflector metasurface consisting of V-shaped gold antennas. The crystal cell is colored yellow [144]. (b) Angular dependence of the deflected beam intensity measured depending on the cell size Γ. The orange and black curves correspond to measurements with and without a polarization filter, respectively. A polarizer was used to separate a deflected beam polarized perpendicular to the incident beam [144]. (c) Intensity profile (on the logarithmic scale) of a vortex beam produced by a metasurface [145]. (d) Interferogram of a beam demonstrating the characteristic branching of the intensity maxima [145]. (e) Reconstructed beam phase at a distance of 4 cm from the metasurface [145]. (f) Image of a TiO$_2$ surface for saturated color microimages [146]. (g) Measured and calculated reflection spectra of samples of different colors [146]. (h) Obtained colors on a standard color CIE 1931 palette [146].

optical vortex with the parameters shown in Figs 11c–e. The interferogram exhibits a fork in the dislocation of maxima, which is typical for vortex states [150].

Metasurfaces are used for manufacturing subwave-length-thick holographic plates [152], polarizers [153], transmitted or reflected beam directors [144], plane lenses [154] and other optical elements. In addition, the resonance elements of metasurfaces can selectively reflect light of certain frequencies, which opens up the opportunity to create saturated high-resolution color figures [146]. Figures 11f–h show the metasurface, providing imaging with a resolution of 16,000 dpi (dots per inch).
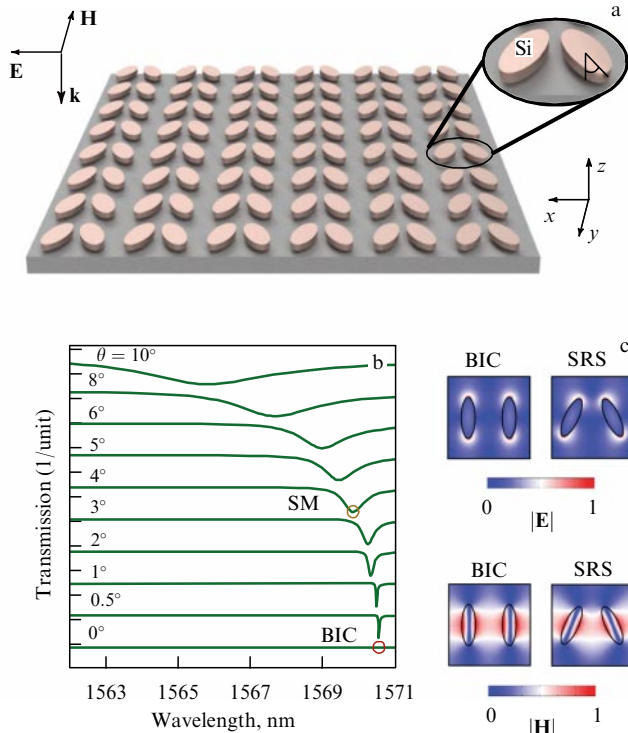
Figure 12. (Color online.) (a) Metasurface consisting of pairs of silicon resonators with ellipsoidal profiles with major axes directed at the angle $\pm\theta$ to the y axis. The square lattice constant is 1320 nm, the ellipse semiaxes are 330 and 110 nm, the height is 200 nm, and the distance between ellipses is 600 nm. (b) Transmission spectra depending on the angle θ. Spectra are displaced vertically by 1.5 units. (c) Distributions of the electric and magnetic fields for a bound state in the continuum (BIC) and a supercavity mode (SM) [155].

Figure 13. (Color online.) Amplifying metasurfaces for magnetic resonance imaging. MRI images obtained without using (a) and using (b) a metasurface with the signal accumulation time of 20 min. MRI images obtained without using (c) and using (d) a metasurface with the signal accumulation time of 2 min. One can see that metasurfaces accelerate the MRI study by an order of magnitude. (e) Photograph of the MRI of a human head using a metasurface. (f, g) Diagram of a hybrid metasurface consisting of a material with a high refractive index (f) combined with metal antennas (g). (h) Calculated distributions of the magnetic (on the left) and electric (on the right) fields near a metasurface shown by a thin blue rectangle elongated along the y axis. The operating amplification region is indicated by a dashed rectangle. (Figs 13a–d [18], Figs e–h [151]).

The arrangement of resonance scatterers in the form of a periodic lattice can lead to the formation of BICs close to those discussed in Section 2.4. BICs can appear on metasurfaces due to the resonance modes of individual structural elements. Therefore, such states more weakly depend on the number of periods and the wave-vector direction than BICs in photonic-crystal membranes. On metasurfaces consisting of dielectric cylinders connected by bridges, lasing was observed [156], even in samples consisting only of 64 cylinders. As in photonic-crystal membranes, symmetry-protected BICs can appear on metasurfaces (Fig. 12). For metasurfaces formed by elements with the broken inversion symmetry, the parameter characterizing BICs was found to be $Q \propto |p - p_0|^{-\alpha}$, where $\alpha = 2$ [155].

Another interesting area in the use of metasurfaces is the electromagnetic-field redistribution in the near wave zone. The solution to this problem was applied in the magnetic resonance imaging (MRI) of living tissues [18, 151]. To obtain an image, a strong magnetic field is required, while a strong electric field negatively acts on living organisms. A specially prepared metasurface can be used to separate localization regions of the magnetic field inside an organism under study and the electric field outside living tissue (Fig. 13).

5. Photonic phase transition

Historically, for many years it was accepted to consider MMs and PCs as two substantially different classes of hand-made photonic structures which were investigated by different
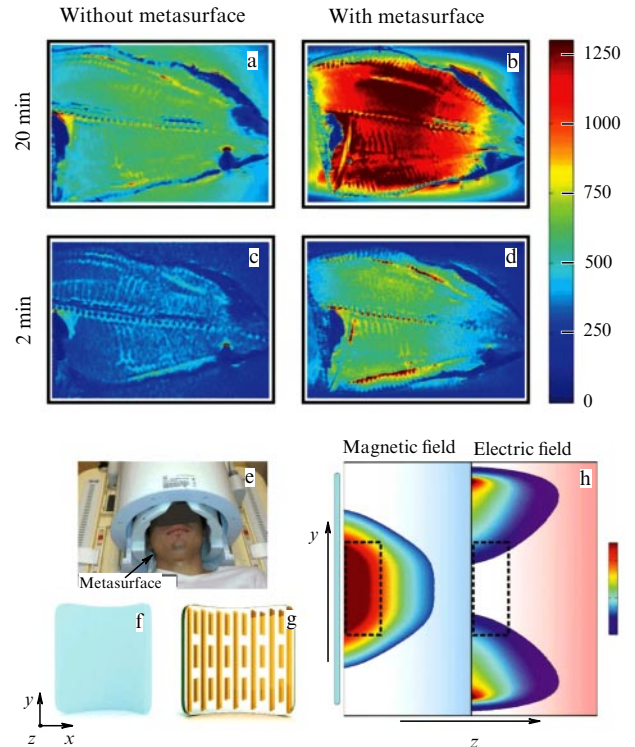
groups presenting the results of their studies at different conferences. However, some materials that are commonly assigned either to PCs or MMs have much in common in their structure, electromagnetic properties, and practical applications. O'Brien and Pendry [27] have shown theoretically that MMs with the effective negative permeability can be created based on a periodic structure consisting of elements with positive permittivity, i.e., based on PCs. It was found that the square lattice of cylinders with a high permittivity ($\varepsilon = 200$) has a negative permeability $\mu < 0$ in the spectral region corresponding to the Mie resonance. At the same time, a similar structure of cylinders with low permittivity ($\varepsilon \approx 4$) is a classical PC [38]. Thus, as the permittivity is changed, the photonic structure acquires negative permeability. It is known that the appearance of new physical properties of materials (first of all, for quantities called the 'generalized susceptibility' in classical textbook [157]) observed upon changing some parameters is commonly related to phase transitions.

Recall that PC properties are determined by Bragg scattering related to the structure periodicity. At the Brillouin zone boundary, the so-called light cones corresponding to the modes of electromagnetic waves in the uniform space split at the intersection point to form the Bragg band gap
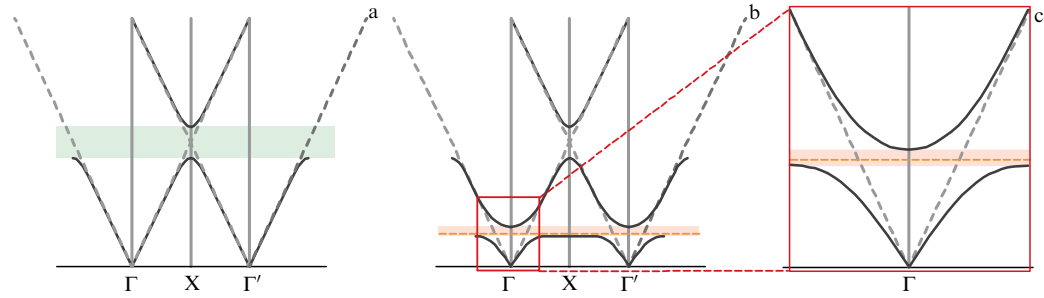
Figure 14. (Color online). (a) Formation scheme of a Bragg stop-band determining the PC properties for wave vectors in the interval $\Gamma - X - \Gamma'$ (Γ' is the point Γ displaced by the reciprocal lattice vector). Dashed straight lines are the projections of unperturbed light cones on the ω, k plane. Solid curves are the PC eigenstates. (b) Formation scheme of a band gap related to the local resonance in an MM. The grey dashed curve is the projection of unperturbed light cones. The orange horizontal dashed line is the unperturbed local state. Solid curves are the photon MM eigenstates. (c) Band gap related to the local state at an enlarged scale [158].

(Fig. 14a). In metamaterials, the fundamental (lowest-frequency) band gap is formed due to interaction between the local resonance and light cone (Figs 14b, c). Unlike the band gap in PCs, the band gap in MMs lies inside the Brillouin zone (Figs 14b, c). The band diagrams of MMs (see, for example, [27, 122]) have the form shown in Fig. 14c.

5.1 Construction of a photonic phase diagram
The authors of Ref. [27] determined the permeability $\mu < 0$ of an MM with the square lattice consisting of dielectric cylinders using transmission and reflection spectra. Subsequent studies showed significant disadvantages of this method of photonic-structure homogenization [132]. In particular, the dispersion curves of effective parameters from [27] do not correspond to the causality principle and, in addition, the value of μ depends on the number of lattice periods. Nevertheless, the main obstacle to structure homogenization is the spatial dispersion. A strong spatial dispersion is observed at the frequencies of Bragg band gaps, while at lower frequencies, including regions with $\mu < 0$, the homogenization is not meaningless. Thus, the photonic structure can be assigned to the MM class when the band gap related to $\mu < 0$ is located below the Bragg band gap. Note that the interpretation of calculated and experimental data is complicated by the fact that in the case of close values of the Bragg frequency and the frequency of local resonance, the Bragg band gap and, therefore, the strong spatial dispersion region considerably broaden [64, 65], which corresponds to the case of resonance PCs discussed in Section 2.

As the structure parameters (the lattice constant and permittivity of cylinders) are continuously varied, the photonic band diagram qualitatively changes, which is accompanied by changes in electromagnetic properties, in particular, by the appearance of negative magnetic susceptibility in a certain spectral interval. Thus, the passage from PCs to MMs studied in papers [39, 159] can be called a photonic phase transition.

Note that the question of the choice of the structure homogenization method was not discussed in [39], but the relation between the band gap and the negative response of the magnetic Mie resonance is beyond question. This follows from three independent series of calculations of (1) the spectra of resonance Mie scattering by a single cylinder, (2) the band diagrams of an infinite crystal, and (3) the transmission spectra of a finite sample. A results of three series completely agree with each other. The map of band gaps depending on ε
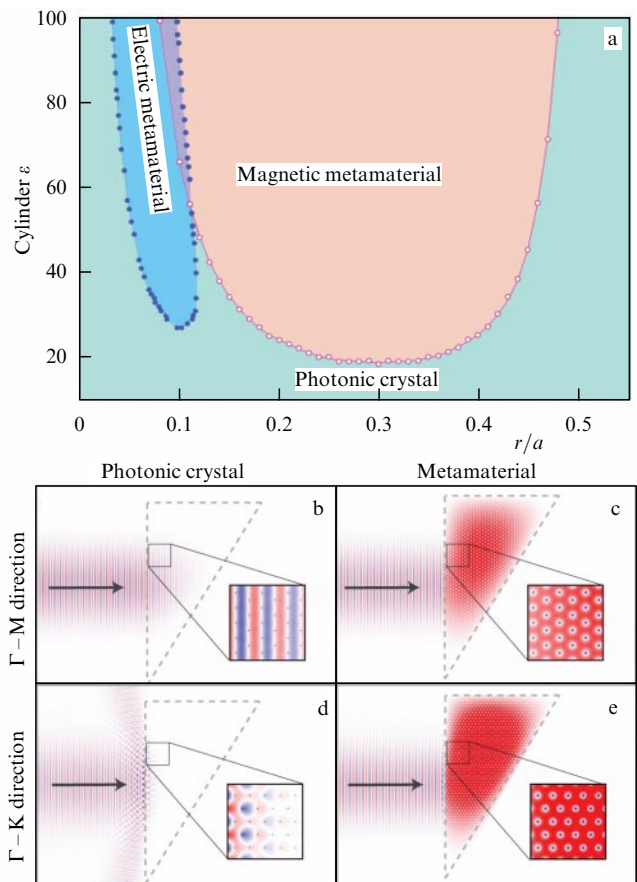

Figure 15. (a) Photonic crystal–metamaterial phase diagram for two-dimensional structures with a square lattice formed by dielectric cylinders in the TE (magnetic MM) and TM (electric MM) polarizations. Dots show points in which the forbidden Mie TE_{01} band splits off from the Bragg stop band, becoming the fundamental forbidden band in the frequency spectrum (figure adapted from [39, 159]). (b–e) Electric field distribution in a prism consisting of dielectric cylinders with $r/a = 0.07$ in two states: (b, d) photonic crystal with $\varepsilon = 8$, $a/\lambda = 0.575$ and (c, e) metamaterial with $\varepsilon = 40$, $a/\lambda = 0.505$ for two light propagation directions: $\Gamma - M$ (b, c) and $\Gamma - K$ (d, e) [160].

demonstrates the splitting off of the lowest-frequency Mie band gap (TE_{01} in the TE polarization and TM_{01} in the TM polarization) and its transformation into the fundamental photonic MM band gap. Based on analysis of calculated data, photonic crystal–metamaterial phase diagrams were con-
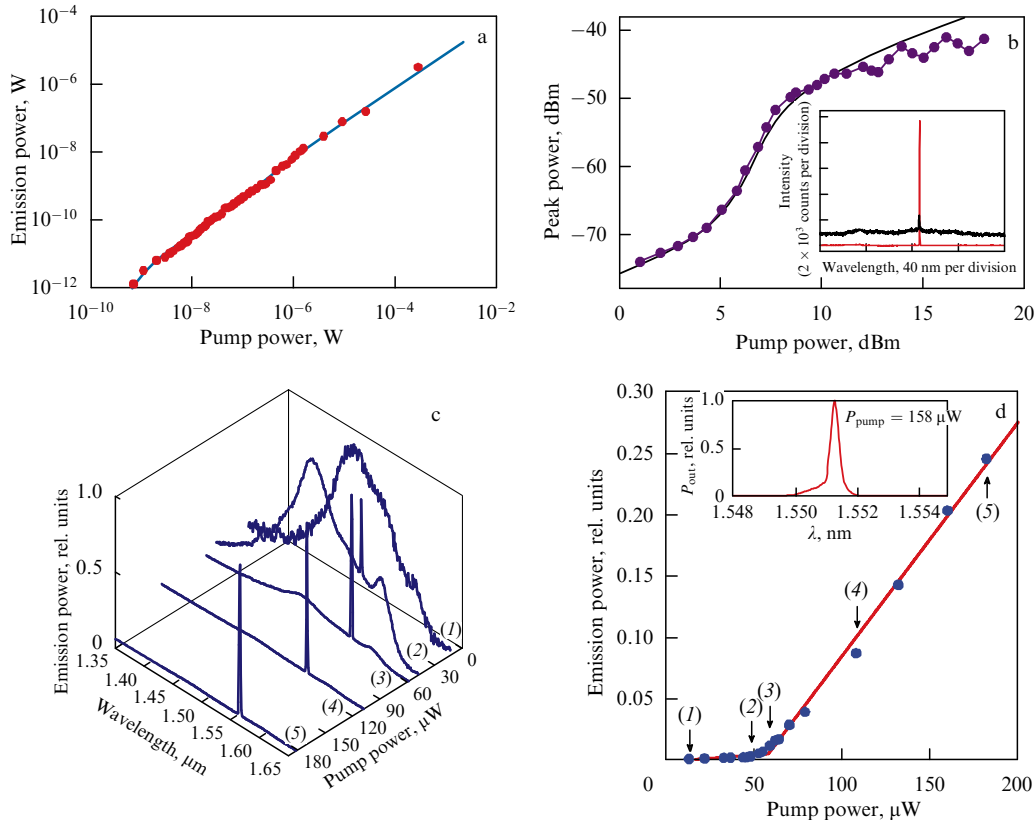
Figure 16. (Color online.) (a) Demonstration of thresholdless lasing in a coaxial nanoresonator at 4.5 K [161]. (b) Peak output power of a Fano laser as a function of the pump power. Blue dots are experimental data; black curve is the approximation of the experiment by a kinetic equation giving the spontaneous emission level of 1%. The inset shows the line spectrum for the pump power of 7.5 dBm (red curve) and 3 dBm (black curve). For clarity, the black curve is displaced along the vertical. In addition, the spectrometer acquisition time is 12 times longer than that during the recording of the red curve [162]. (c) Lasing on a metasurface in the BIC regime [156]. Transformation of the normalized emission spectrum into the 1551.4-nm laser line upon increasing the pump power. (d) Output power as a function of the pump power in the laser line region. The inset shows the laser line for the 158-μW pump power. The measured linewidth of 0.33 nm is limited by the instrumental function [156].

structed in coordinates r/a and ε for the TE polarization ('magnetic MM'; the magnetic field oscillates along the cylinder axis [39]) and the TM polarization ('electric MM'; the electric field oscillates along the cylinder axis [159]) (Fig. 15a).

The diagram allows one to determine certainly whether the structure belongs to the PC class (the fundamental band gap is related to the Bragg resonance) or to the MM class (the fundamental band gap is related to local Mie resonances in dielectric cylinders). In this case, the band gap in the resonance region determined the frequency interval with the negative magnetic susceptibility in the initially dielectric structure, which reliably confirms the interpretation of the observed phenomena as a phase transition of a new type.

To demonstrate the possibility of homogenization of the structure in the MM phase, we calculated field distributions in samples in the form of a triangular prism consisting of dielectric cylinders with square [159] and simple triangular lattices. The electric field intensity distribution was calculated for a Gaussian beam incident on a prism along the $\Gamma-M$ and $\Gamma-K$ directions (Figs 15b–e). In the photonic-crystal phase ($\varepsilon = 8$), the field has the 'striped' shape typical of PCs (the field in adjacent cells oscillates out-of-phase). For the $\Gamma-K$ direction, the frequency $a/\lambda = 0.575$ falls into the stop-band, and an exponential decay of the light beam is observed. Thus, the field distribution is inhomogeneous and considerably depends on the orientation of the PC axes. In the MM regime

($\varepsilon = 40$), the field distribution at the frequency $a/\lambda = 0.505$ is homogeneous over the entire structure (the field in adjacent cells oscillated in phase) and is independent of the orientation of crystal axes.

5.2 Preparation of dielectric metamaterials

The experimental observation of a photonic phase transition and the preparation of a dielectric MM were reported in [39]. The sample was a lattice of plastic tubes fixed in a system of movable holders allowing a change in the parameter r/a in experiments by retaining the square system of the 2D photonic structure. The sample permittivity was varied by filling the tubes with water, which in the microwave range has a strong temperature dependence $\varepsilon(T) = 50-80$ in the range of $T = 20-90\,°C$. The transmission spectra of this structure were measured as functions of parameters r/a and ε. Experimental data were in good agreement with calculations, including the observation of the lowest Mie mode splitting off from the Bragg band gap, i.e., the PC → MM phase transition.

Photonic crystal–metamaterial phase diagrams for structures made of silicon cylinders were presented in [158]. In particular, a structure with a triangular lattice was considered in which the minimal frequency of Bragg resonances is higher than that for a square lattice. For this reason, the silicon structure with the permittivity $\varepsilon > 13.5$ in the spectral interval $\lambda < 800$ nm can pass to the magnetic MM phase.

6. Conclusions

Note in conclusion that, despite numerous papers devoted to the study of resonance effects in photonic structures, publications of new nontrivial results should be expected in the nearest future. These results can be quite unexpected, like lasing in a plasmonic structure with the mode size two orders of magnitude smaller than the diffraction limit [163] or thresholdless lasing in coaxial resonators [161] (Fig. 16a).

Indeed, most of the areas of nanophotonics which have appeared in recent years are related to various resonance phenomena. We will list here only some original results: observation of the Fano resonance in topological Bi_2Se_3 and $(Bi_{1-x}In_x)_2Se_3$ insulators [164, 165], broadband tuning of mechanical resonances with the help of plasmonic MMs [21], optical switching in resonance plasmon-atomic systems [166], an ultrashort pulse laser emitting in the gigahertz range based on resonance between the guided mode and the structural defect mode (a Fano laser) [162] (Fig. 16b), the elastic Purcell effect in nanoparticles [167], resonance sensors to identify molecular monolayers [168], spectral separation of optical spins based on Fano resonance [169], lasing on a metasurface [156] (Figs 16c, d), and a number of other papers cited in this review. It is also necessary to mention nonlinear structures raising the functional properties of PCs and MMs to a new level. Various lasing and mixing regimes that can be achieved on nonlinear metasurfaces are considered in [170].

We discussed in this review various resonance phenomena, most of which can be interpreted within the framework of a simple model based on two coupled mechanical oscillators [60]. Based on this model, a phase diagram was proposed with axes corresponding to the decay rates of oscillators. The phase diagram shows, in particular, the regions of existence of various resonance regimes corresponding to the weak (Fano resonance, electromagnetically induced transparency, Kerker and Borrmann effects) and strong coupling (*PT*-symmetry breaking). A distinct knowledge of the characteristic features of each resonance effect is a key factor for the successful design of reliable functional photonic devices.

References

1. John S *Phys. Rev. Lett.* **58** 2486 (1987)
2. Yablonovitch E *Phys. Rev. Lett.* **58** 2059 (1987)
3. Rayleigh Lord *Phil. Mag. 5* **24** 145 (1887)
4. Bykov V P *Sov. Phys. JETP* **35** 369 (1972); *Zh. Eksp. Teor. Fiz.* **62** 505 (1972)
5. Pendry J B et al. *Phys. Rev. Lett.* **76** 4773 (1996)
6. Pendry J B et al. *IEEE Trans. Microwave Theory Tech.* **47** 2075 (1999)
7. Markoš P, Soukoulis C M *Phys. Rev. B* **65** 033401 (2001)
8. Engheta N, Ziolkowski R W (Eds) *Electromagnetic Metamaterials: Physics and Engineering Explorations* (New York: Wiley–IEEE Press, 2006)
9. Capolino F (Ed.) *Theory and Phenomena of Metamaterials* (Boca Raton, FL: CRC Press–Taylor and Francis, 2009)
10. Sarychev A K, Shalaev V M *Electrodynamics of Metamaterials* (Singapore: World Scientific, 2007); Translated into Russian: *Elektrodinamika Metamaterialov* (Moscow: Nauchnyi Mir, 2011)
11. Veselago V G *Sov. Phys. Usp.* **10** 509 (1968); *Usp. Fiz. Nauk* **92** 517 (1967)
12. Linden S et al. *Science* **306** 1351 (2004)
13. Fang N et al. *Science* **308** 534 (2005)
14. Liu Z et al. *Science* **315** 1686 (2007)
15. Pendry J B, Schurig D, Smith D R *Science* **312** 1780 (2006)
16. Chen P-Y, Soric J, Alù A *Adv. Mater.* **24** OP281 (2012)
17. Rybin M V et al. *Sci. Rep.* **5** 8774 (2015)
18. Slobozhanyuk A P et al. *Adv. Mater.* **28** 1832 (2016)
19. Tittl A et al. *Science* **360** 1105 (2018)
20. Landy N I et al. *Phys. Rev. Lett.* **100** 207402 (2008)
21. Zhu H, Yi F, Cubukcu E *Nature Photon.* **10** 709 (2016)
22. Smith D R et al. *Phys. Rev. Lett.* **84** 4184 (2000)
23. Parazzoli C G et al. *Phys. Rev. Lett.* **90** 107401 (2003)
24. Valentine J et al. *Nature* **455** 376 (2008)
25. Kildishev A V, Boltasseva A, Shalaev V M *Science* **339** 1232009 (2013)
26. Yu N, Capasso F *Nature Mater.* **13** 139 (2014)
27. O'Brien S, Pendry J B *J. Phys. Condens. Matter* **14** 4035 (2002)
28. Kuznetsov A I et al. *Sci. Rep.* **2** 492 (2012)
29. Moitra P et al. *Nature Photon.* **7** 791 (2013)
30. Yang Y et al. *Nature Commun.* **5** 5753 (2014)
31. Jahani S, Jacob Z *Nature Nanotechnol.* **11** 23 (2016)
32. Kuznetsov A I et al. *Science* **354** aag2472 (2016)
33. Staude I, Schilling J *Nature Photon.* **11** 274 (2017)
34. Vlasov Yu A et al. *Nature* **414** 289 (2001)
35. López J F G, López C, in *Optical Properties of Photonic Structures: Interplay of Order and Disorder* (Boca Raton, FL: CRC Press–Taylor and Francis, 2016) p. 197
36. Galisteo-López J F et al. *Phys. Rev. B* **68** 115109 (2003)
37. Sakoda K *Optical Properties of Photonic Crystals* 2nd ed. (Berlin: Springer, 2005)
38. Joannopoulos J D et al. *Photonic Crystals: Molding the Flow of Light* 2nd ed. (Princeton, NJ: Princeton Univ. Press, 2008)
39. Rybin M V et al. *Nature Commun.* **6** 10102 (2015)
40. Ashcroft N W, Mermin N D *Solid State Physics* Vol. 1 (New York: Holt, Rinehart and Winston, 1976); Translated into Russian: *Fizika Tverdogo Tela* Vol. 1 (Moscow: Mir, 1979)
41. Shishkin I I et al. *Phys. Rev. B* **89** 035124 (2014)
42. Zakhidov A A et al. *Science* **282** 897 (1998)
43. Astratov V N et al. *Nuovo Cimento D* **17** 1349 (1995)
44. Miguez H et al. *Appl. Phys. Lett.* **71** 1148 (1997)
45. Mazurenko D A et al. *Phys. Rev. Lett.* **91** 213903 (2003)
46. Wijnhoven J E G J, Vos W L *Science* **281** 802 (1998)
47. Romanov S G et al. *Phys. Rev. E* **63** 056603 (2001)
48. Galisteo-López J F et al. *Photon. Nanostruct. Fundament. Appl.* **2** 117 (2004)
49. van Driel H M, Vos W L *Phys. Rev. B* **62** 9872 (2000)
50. Gajiev G M et al. *Phys. Rev. B* **72** 205115 (2005)
51. Baryshev A V et al. *Phys. Rev. B* **76** 014305 (2007)
52. Moroz A V, Limonov M F, Rybin M V, Samusev K B *Phys. Solid State* **53** 1105 (2011); *Fiz. Tverd. Tela* **53** 1045 (2011)
53. Rybin M V et al. *Phys. Rev. Lett.* **103** 023901 (2009)
54. García P D, Sapienza R, López C *Adv. Mater.* **22** 12 (2010)
55. Hendrickson J et al. *Opt. Express* **16** 15382 (2008)
56. Baryshev A V et al. *Phys. Rev. Lett.* **99** 063906 (2007)
57. Rybin M V et al. *Phys. Rev. B* **77** 205106 (2008)
58. Miroshnichenko A E, Flach S, Kivshar Y S *Rev. Mod. Phys.* **82** 2257 (2010)
59. Luk'yanchuk B et al. *Nature Mater.* **9** 707 (2010)
60. Limonov M F, Rybin M V, Poddubny A N, Kivshar Y S *Nature Photon.* **11** 543 (2017)
61. Fano U *Phys. Rev.* **124** 1866 (1961)
62. Connerade J-P, Lane A M *Rep. Prog. Phys.* **51** 1439 (1988)
63. Poddubny A N, Rybin M V, Limonov M F, Kivshar Y S *Nature Commun.* **3** 914 (2012)
64. Ivchenko E L et al. *Phys. Rev. B* **70** 195106 (2004)
65. Ivchenko E L, Poddubny A N *Phys. Solid State* **55** 905 (2013); *Fiz. Tverd. Tela* **55** 833 (2013)
66. Poddubny A N, Ivchenko E L *Physica E* **42** 1871 (2010)

67. Poddubny A N et al. *Phys. Rev. B* **80** 115314 (2009)
68. Poddubny A N et al. *Phys. Rev. B* **77** 113306 (2008)
69. Werchner M et al. *Opt. Express* **17** 6813 (2009)
70. Goto T et al. *Phys. Rev. Lett.* **101** 113902 (2008)
71. Vinogradov A P et al. *Phys. Usp.* **53** 243 (2010); *Usp. Fiz. Nauk* **180** 249 (2010)
72. Tikhodeev S G, Gippius N A *Phys. Usp.* **52** 945 (2009); *Usp. Fiz. Nauk* **179** 1003 (2009)
73. Hsu C W et al. *Nature* **499** 188 (2013)
74. Yang Y et al. *Phys. Rev. Lett.* **113** 037401 (2014)
75. von Neuman J, Wigner E *Phys. Z.* **30** 467 (1929)
76. Lee J et al. *Phys. Rev. Lett.* **109** 067401 (2012)
77. Friedrich H, Wintgen D *Phys. Rev. A* **32** 3231 (1985)
78. Rybin M, Kivshar Yu *Nature* **541** 164 (2017)
79. Krasikov S D, Bogdanov A A, Iorsh I V *Phys. Rev. B* **97** 224309 (2018)
80. Hirose K et al. *Nature Photon.* **8** 406 (2014)
81. Mühlschlegel P et al. *Science* **308** 1607 (2005)
82. Liu N et al. *Nature Mater.* **10** 631 (2011)
83. Makarov S V et al. *Nano Lett.* **17** 3047 (2017)
84. Schelkunoff S A, Friis H T *Antennas. Theory and Practice* (New York: Wiley, 1952); Translated into Russian: *Antenny. Teoriya i Praktika* (Moscow: Sov. Radio, 1955)
85. Novotny L, van Hulst N *Nature Photon.* **5** 83 (2011)
86. Krasnok A E et al. *Phys. Usp.* **56** 539 (2013); *Usp. Fiz. Nauk* **183** 561 (2013)
87. Meinzer N, Barnes W L, Hooper I R *Nature Photon.* **8** 889 (2014)
88. Taminiau T H et al. *Nano Lett.* **7** 28 (2007)
89. Large N et al. *Nano Lett.* **10** 1741 (2010)
90. Kim S et al. *Nature* **453** 757 (2008)
91. Kinkhabwala A et al. *Nature Photon.* **3** 654 (2009)
92. Rybin M V et al. *Opt. Express* **21** 30107 (2013)
93. Tribelsky M I, Miroshnichenko A E *Phys. Rev. A* **93** 053837 (2016)
94. Klimov V V, Ducloy M, Letokhov V S *Phys. Rev. A* **59** 2996 (1999)
95. Bakker R M et al. *Nano Lett.* **15** 2137 (2015)
96. Lu G et al. *Laser Photon. Rev.* **9** 530 (2015)
97. Yan J et al. *ACS Nano* **9** 2968 (2015)
98. Xi Z et al. *Phys. Rev. Lett.* **117** 113903 (2016)
99. King R W P, Fikioris G J, Mack R B *Cylindrical Antennas and Arrays* 2nd ed. (Cambridge: Cambridge Univ. Press, 2002)
100. Li J, Salandrino A, Engheta N *Phys. Rev. B* **76** 245403 (2007)
101. Curto A G et al. *Science* **329** 930 (2010)
102. Dorfmüller J et al. *Nano Lett.* **11** 2819 (2011)
103. Krasnok A E et al. *Opt. Express* **20** 20599 (2012)
104. Filonov D S et al. *Appl. Phys. Lett.* **100** 201113 (2012)
105. Rybin M V et al. *Phys. Rev. B* **88** 205106 (2013)
106. Tribelsky M I et al. *Phys. Rev. Lett.* **100** 043903 (2008)
107. Tribelsky M I, Miroshnichenko A E, Kivshar Y S *Europhys. Lett.* **97** 44005 (2012)
108. Kong X, Xiao G *J. Opt. Soc. Am. A* **33** 707 (2016)
109. Rituraj, Catrysse P B, Fan S *Opt. Express* **27** 3991 (2019)
110. Leonhardt U *Science* **312** 1777 (2006)
111. Kildishev A V, Shalaev V M *Phys. Usp.* **54** 53 (2011); *Usp. Fiz. Nauk* **181** 59 (2011)
112. Zharova N A et al. *Opt. Express* **20** 14954 (2012)
113. Chen P-Y, Alù A *ACS Nano* **5** 5855 (2011)
114. Kort-Kamp W J M et al. *Phys. Rev. Lett.* **111** 215504 (2013)
115. Ruan Z, Fan S *J. Phys. Chem. C* **114** 7324 (2010)
116. Edwards B et al. *Phys. Rev. Lett.* **103** 153901 (2009)
117. Rybin M V et al. *Phys. Rev. Lett.* **119** 243901 (2017)
118. Van Bladel J *IEEE Trans. Microwave Theory Tech.* **23** 199 (1975)
119. Carletti L et al. *Phys. Rev. Lett.* **121** 033903 (2018)
120. Bogdanov A A et al. *Adv. Photon.* **1** 016001 (2019)
121. Kaatze U *J. Chem. Eng. Data* **34** 371 (1989)
122. Ramakrishna S A *Rep. Prog. Phys.* **68** 449 (2005)
123. Landau L D, Lifshitz E M *Electrodynamics of Continuous Media* (Oxford: Pergamon Press, 1984); Translated from Russian: *Elektrodinamika Sploshnykh Sred* (Moscow: Fizmatlit, 2013)
124. Johnson P B, Christy R W *Phys. Rev. B* **6** 4370 (1972)
125. Aspnes D E, Studna A A *Phys. Rev. B* **27** 985 (1983)
126. Shelby R A et al. *Appl. Phys. Lett.* **78** 489 (2001)
127. Shelby R A, Smith D R, Schultz S *Science* **292** 77 (2001)
128. Zywietz U et al. *Nature Commun.* **5** 3402 (2014)
129. Dorofeenko A V et al. *Phys. Usp.* **55** 1080 (2012); *Usp. Fiz. Nauk* **182** 1157 (2012)
130. Vinogradov A P, Dorofeenko A V, Zukhdi S *Phys. Usp.* **51** 485 (2008); *Usp. Fiz. Nauk* **178** 511 (2008)
131. Vinogradov A P *Elektrodinamika Kompozitnykh Materialov* (Electrodynamics of Composite Materials) (Moscow: Editorial URSS, 2001)
132. Simovski C R *Opt. Spectrosc.* **107** 726 (2009); *Opt. Spektrosk.* **107** 766 (2009)
133. Feynman R P, Leighton R B, Sands M *The Feynman Lectures on Physics* Vol. 3 (Reading, Mass.: Addison-Wesley, 1965); Translated into Russian: *Feinmanovskie Lektsii po Fizike* Vol. 3 (Moscow: Editorial URSS, 2016)
134. Jackson J D *Classical Electrodynamics* 3rd ed. (New York: Wiley, 1999)
135. Xu L, Chen H *Nature Photon.* **9** 15 (2015)
136. Dubinov A E, Mytareva L A *Phys. Usp.* **53** 455 (2010); *Usp. Fiz. Nauk* **180** 475 (2010)
137. Wolf E, Habashy T *J. Mod. Opt.* **40** 785 (1993)
138. Rozanov N N *Phys. Usp.* **54** 763 (2011); *Usp. Fiz. Nauk* **181** 787 (2011)
139. Dubinov A E, Mytareva L A *Phys. Usp.* **55** 315 (2012); *Usp. Fiz. Nauk* **182** 337 (2012)
140. Shchelokova A V et al. *Phys. Usp.* **58** 167 (2015); *Usp. Fiz. Nauk* **185** 181 (2015)
141. Schurig D et al. *Science* **314** 977 (2006)
142. Guven K et al. *New J. Phys.* **10** 115037 (2008)
143. Semouchkina E et al. *Appl. Phys. Lett.* **96** 233503 (2010)
144. Yu N et al. *Science* **334** 333 (2011)
145. Chong K E et al. *Nano Lett.* **15** 5369 (2015)
146. Sun S et al. *ACS Nano* **11** 4445 (2017)
147. Pendry J B et al. *Science* **337** 549 (2012)
148. Sheng C et al. *Nature Photon.* **7** 902 (2013)
149. Remnev M A, Klimov V V *Phys. Usp.* **61** 157 (2018); *Usp. Fiz. Nauk* **188** 169 (2018)
150. Berry M V et al. *Eur. J. Phys.* **1** 154 (1980)
151. Schmidt R et al. *Sci. Rep.* **7** 1678 (2017)
152. Ni X, Kildishev A V, Shalaev V M *Nature Commun.* **4** 2807 (2013)
153. Guo T, Argyropoulos C *Opt. Lett.* **41** 5592 (2016)
154. Khorasaninejad M et al. *Nano Lett.* **15** 5358 (2015)
155. Koshelev K et al. *Phys. Rev. Lett.* **121** 193903 (2018)
156. Kodigala A et al. *Nature* **541** 196 (2017)
157. Landau L D, Lifshitz E M *Statistical Physics* Vol. 1 (Oxford: Pergamon Press, 1980); Translated from Russian: *Statisticheskaya Fizika* Pt. 1 (Moscow: Fizmatlit, 2013)
158. Li S V, Kivshar Y S, Rybin M V *ACS Photon.* **5** 4751 (2018)
159. Maslova E E, Limonov M F, Rybin M V *Opt. Lett.* **43** 5516 (2018)
160. Maslova E E, Limonov M F, Rybin M V *JETP Lett.* **109** 340 (2019); *Pis'ma Zh. Eksp. Teor. Fiz.* **109** 347 (2019)
161. Khajavikhan M et al. *Nature* **482** 204 (2012)
162. Yu Y et al. *Nature Photon.* **11** 81 (2017)
163. Oulton R F et al. *Nature* **461** 629 (2009)
164. Tung L-C et al. *Phys. Rev. B* **93** 085140 (2016)
165. Glinka Y D et al. *J. Phys. Condens. Matter* **28** 165601 (2016)
166. Stern L, Grajower M, Levy U *Nature Commun.* **5** 4865 (2014)
167. Schmidt M K et al. *Phys. Rev. Lett.* **121** 064301 (2018)
168. Wu C et al. *Nature Mater.* **11** 69 (2012)
169. Piao X et al. *Sci. Rep.* **5** 16585 (2015)
170. Krasnok A, Tymchenko M, Alù A *Mater. Today* **21** (1) 8 (2018)